ACS central science

Research Article

http://pubs.acs.org/journal/acscii

Mesoporous TiO_2 Mesocrystals: Remarkable Defects-Induced Crystallite-Interface Reactivity and Their in Situ Conversion to Single Crystals

Yong Liu,[†] Yongfeng Luo,[†,‡] Ahmed A. Elzatahry,[§] Wei Luo,[†,⊥] Renchao Che,[†] Jianwei Fan,[†,#] Kun Lan,[†] Abdullah M. Al-Enizi,[▽] Zhenkun Sun,[†] Bin Li,[†] Zhengwang Liu,[†] Dengke Shen,[†] Yun Ling,[†] Chun Wang,[†] Jingxiu Wang,[†] Wenjun Gao,[†] Chi Yao,[†] Kaiping Yuan,[†] Huisheng Peng,[○] Yun Tang,[†] Yonghui Deng,[†] Gengfeng Zheng,[†] Gang Zhou,[†] and Dongyuan Zhao*[,†]

[†]Department of Chemistry, Shanghai Key Laboratory of Molecular Catalysis and Innovative Materials, State Key Laboratory of Molecular Engineering of Polymers, Laboratory of Advanced Materials, Fudan University, Shanghai, 200433, China

[‡]College of Science, Central South University of Forestry and Technology, Changsha, Hunan 410004, China

[§]Materials Science and Technology Program, College of Arts and Sciences, Qatar University, P.O. Box 2713, Doha, Qatar

[⊥]State Key Laboratory for Modification of Chemical Fibers and Polymer Materials, College of Materials Science and Engineering, Donghua University, Shanghai 201620, P. R. China

[#]College of Environmental Science and Engineering, State Key Laboratory of Pollution Control and Resource Reuse, Tongji University, Shanghai 200092, P. R. China

[▽]Department of Chemistry, College of Science, King Saud University, Riyadh 11451, Saudi Arabia

[○]State Key Laboratory of Molecular Engineering of Polymers, Department of Macromolecular Science, and Laboratory of Advanced Materials, Fudan University, Shanghai 200438, China

S *Supporting Information*

ABSTRACT: Oriented self-assembly between inorganic nanocrystals and surfactants is emerging as a route for obtaining new mesocrystalline semiconductors. However, the actual synthesis of mesoporous semiconductor mesocrystals with abundant surface sites is extremely difficult, and the corresponding new physical and chemical properties arising from such an intrinsic porous mesocrystalline nature, which is of fundamental importance for designing high-efficiency nanostructured devices, have been rarely explored and poorly understood. Herein, we report a simple evaporation-driven oriented assembly method to grow unprecedented olive-shaped mesoporous TiO_2 mesocrystals (FDU-19) self-organized by ultrathin flake-like anatase nanocrystals (~8 nm in thickness). The mesoporous mesocrystals FDU-19 exhibit an ultrahigh surface area (~189 m^2/g), large internal pore volume (0.56 cm^3/g), and abundant defects (oxygen vacancies or unsaturated Ti^{3+} sites), inducing remarkable crystallite-interface reactivity. It is found that the mesocrystals FDU-19 can be easily fused in situ into mesoporous anatase single crystals (SC-FDU-19) by annealing in air. More significantly, by annealing in a vacuum (~4.0×10^{-5} Pa), the mesocrystals experience an abrupt three-dimensional to two-dimensional structural transformation to form ultrathin anatase single-crystal nanosheets (NS-FDU-19, ~8 nm in thickness) dominated by nearly 90% exposed reactive (001) facets. The balance between attraction and electrostatic repulsion is proposed to determine the resulting geometry and dimensionality. Dye-sensitized solar cells based on FDU-19 and SC-FDU-19 samples show ultrahigh photoconversion efficiencies of up to 11.6% and 11.3%, respectively, which are largely attributed to their intrinsic single-crystal nature as well as high porosity. This work gives new understanding of physical and chemical properties of mesoporous semiconductor mesocrystals and opens up a new pathway for designing various single-crystal semiconductors with desired mesostructures for applications in catalysis, sensors, drug delivery, optical devices, etc.

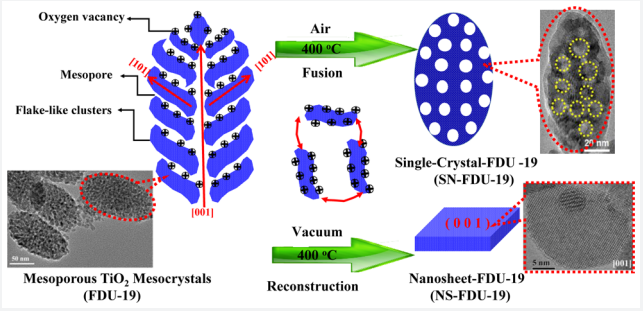

Received: July 15, 2015
Published: September 9, 2015

DOI: 10.1021/acscentsci.5b00256
ACS Cent. Sci. 2015, 1, 400−408

INTRODUCTION

Oriented self-assembly of nanoparticle building blocks and surfactants into ordered superstructures has been the subject of active chemical and materials research.[1−10] Such an anisotropy superstructure is often best described as a mesocrystal: inorganic superstructures made by highly parallel crystallization and controlled alignment, which is first proposed as a new class of ordered nanoparticle superstructures by Cölfen and Antonietti in 2005.[11] The synthesis of this new particle-mediated mesocrystal greatly challenges the classical "ion-mediated" crystallization process.[12−14] Owing to its unique oriented mesostructure and good electronic conductivity, the mesocrystal is an ideal candidate for catalysis, sensing, and energy storage and conversion.[11,15−24] However, if a large number of internal mesopores and active sites are induced, the high porosity and strong interbuilding particle interaction within the mesoscopic structures may change their paradigm of self-organization processes for original nanocrystal building blocks under a certain external stimulation (e.g., heating treatment).[11,25] Unfortunately, the actual synthesis of mesoporous anisotropic mesocrystals with abundant surface sites is extremely difficult because of uncontrollable orientation and assembly of nanocrystal building blocks. The corresponding new unique physical and chemical properties arising from such mesoporous anisotropic superstructures are highly desirable to be further explored and understood, since it is of fundamental importance for designing high-efficiency functional materials in catalysis, sensors, optoelectronic devices, etc.

Herein, we report a simple evaporation-driven oriented assembly method to grow unprecedented olive-shaped mesoporous TiO_2 mesocrystals (FDU-19). This evaporation-driven oriented assembly starts with the liquid−liquid phase separation as the preferential evaporation of tetrahydrofuran (THF) solvent at a low temperature of 60 °C, and uniform olive-shaped three-dimensional (3D) TiO_2 particles assembled by PEO−PPO−PEO/titania oligomer spherical micelles are formed at the liquid−liquid interface (Figure 1a, Figures S1 and S2). Continuous evaporation of the residue THF and hydrolyzed solvents drives the oriented growth of both mesopore channels and flake-like nanocrystals from the initially formed spherical composite micelles along the free radial and restricted tangential direction, yielding 3D-open anisotropic olive-like mesoporous TiO_2 mesocrystals (FDU-19) with very uniform particle size.

RESULTS AND DISCUSSION

The low-magnification scanning electron microscopy (SEM) image (Figure 1b) shows that the typical FDU-19 particles after calcination under N_2 at 350 °C for 2 h have uniform 3D olive-like shape with an average length and width of about 140 and 65 nm, respectively. A high-magnification SEM image reveals that 3D open pores with ∼7 nm diameter are exposed on the rough surface. Transmission electron microscopy (TEM) characterizations (Figure 1c and Figure S3a−e) further demonstrate that the mesopores of FDU-19 particles are distributed radially from the center to the surface, and all of them are highly open. All the mesopore walls are constructed by oriented flake-like anatase nanocrystallites with a thickness of ∼8 nm. It is worth to note that the pore size can be enlarged to be about 15 nm with the aid of 1,3,5-trimethylbenzene (TMB) molecules. However, it is found that adding TMB as a pore expander can deteriorate the oriented assembly of the PEO−PPO−PEO/titania spherical composite micelles at the liquid−liquid phase interface, resulting in irregular mesoporous TiO_2 bulks with a large spherical pore (Figure S4).

The high-resolution TEM (HRTEM) images recorded along the [010] zone clearly show an interfacial angle (68.3°) of the (101) and (002) planes (Figure 1d).[26−30] Meanwhile, HRTEM images recorded along the [001] zone reveal the interfacial angle of (200) and (020) planes to be 90° (Figure S3f).[26,27,31] These results confirm well that all the flake-like anatase frameworks share the [001] crystallographic orientation. Significantly, some dislocations accompanied by edge defects are observed in the area of the crystallite interfaces (Figure 1d and Figure S3g,h). All of the selected area electronic diffraction (SAED) patterns (inset of Figure 1c, and Figure S3c,e) recorded on a single-isolated FDU-19 nanoparticle show identical elongated single-crystal-like diffraction spots, which is attributed to the same crystallographic orientation of flake-like anatase building blocks within FDU-19 nanoparticle. Meanwhile, the diffraction spots are slightly elongated, clearly indicating the dislocations and some lattice mismatches at crystal grain boundaries within the mesoporous FDU-19 mesocrystals.[32−36]

Electron paramagnetic resonance (EPR) spectra of the mesoporous TiO_2 mesocrystals shows a strong signal at g = 2.002 (Figure 1e), confirming the existence of a large amount of oxygen vacancies (unsaturated Ti^{3+} sites).[37] X-ray photoelectron spectrum (XPS) of Ti 2p for FDU-19 mesocrystals (Figure 1f) shows two sets of peaks, which can be well assigned to Ti^{3+} (Ti $2p_{1/2}$ at 462.6 eV, Ti $2p_{3/2}$ at 456.9 eV) and Ti^{4+} (Ti $2p_{1/2}$ at 464.3 eV, Ti $2p_{3/2}$ at 458.6 eV),[38−40] respectively. The ratio of Ti^{3+}/ Ti^{4+} is measured to be as large as 1.4:1, suggesting a high concentration of oxygen vacancies (Ti^{3+} sites) distributed on the mesocrystals. Correspondingly, three main peaks at binding energies of 528.0, 529.5, and 531.6 eV are observed in O 1s XPS spectra, which can be assigned to the lattice oxygen O−Ti^{3+}, O−Ti^{4+} and hydroxyl oxygen (O−H) on the surface (Figure 1g).[41] The Cl 2p signal can clearly be observed at a binding energy of 198.4 eV, which is a typical value for Cl−Ti species,[42] suggesting that Cl^- ions are chemisorbed on the unsaturated Ti^{3+} sites (Figure S5a,b). The thermogravimetry (TG) curve of the FDU-19 mesocrystals conducted in air shows two main loss stages (Figure S5c). The first stage to 200 °C with a 5% loss is caused by dehydration, and the second one with ∼10% loss (200−400 °C) is attributed to the removal of hydroxyl groups (−OH) and Cl^- ions on the mesocrystals. The integrated energy dispersive X-ray spectroscopy (EDS) analysis (Figure S6) confirms the presence of Ti, O, and a small amount of Cl. More significantly, the zeta potential (ζ) of the mesoporous TiO_2 mesocrystals shows a positive (+ 60 mV) peak with several satellite peaks (Figure S7), indicating that the surface charges is mainly positive, but the negative charge partially exists.

The wide-angle X-ray diffraction (WXRD) patterns (Figure 1h) of the mesoporous TiO_2 mesocrystals reveal a highly crystalline anatase phase (space group $I4_1/amd$). The average crystallite size is calculated to be ∼8.5 nm, in agreement with the domain size of the flake-like nanocrystals estimated from the TEM images. Nitrogen adsorption−desorption isotherms show characteristic type IV curves with two distinguishable capillary condensation steps (Figure 1i). A distinct capillary condensation at P/P_0 = 0.40−0.7, reflecting uniform primary mesopore channels of FDU-19 mesocrystals. Moreover, a hysteresis loop at a higher pressure (P/P_0 = 0.90−0.99) probably reveals the interchannel macropores caused from the structural defects. The pore size distribution calculated by the Barrett−Joyner−Halenda (BJH) model (inset of Figure 1i) is centered at about 7.3 nm, consistent with the results from TEM analyses. The Brunauer−Emmett−Teller (BET) surface area and pore volume are calculated to be as high as ∼189 m^2/g and 0.56 cm^3/g, respectively. The average

DOI: 10.1021/acscentsci.5b00256
ACS Cent. Sci. 2015, 1, 400−408

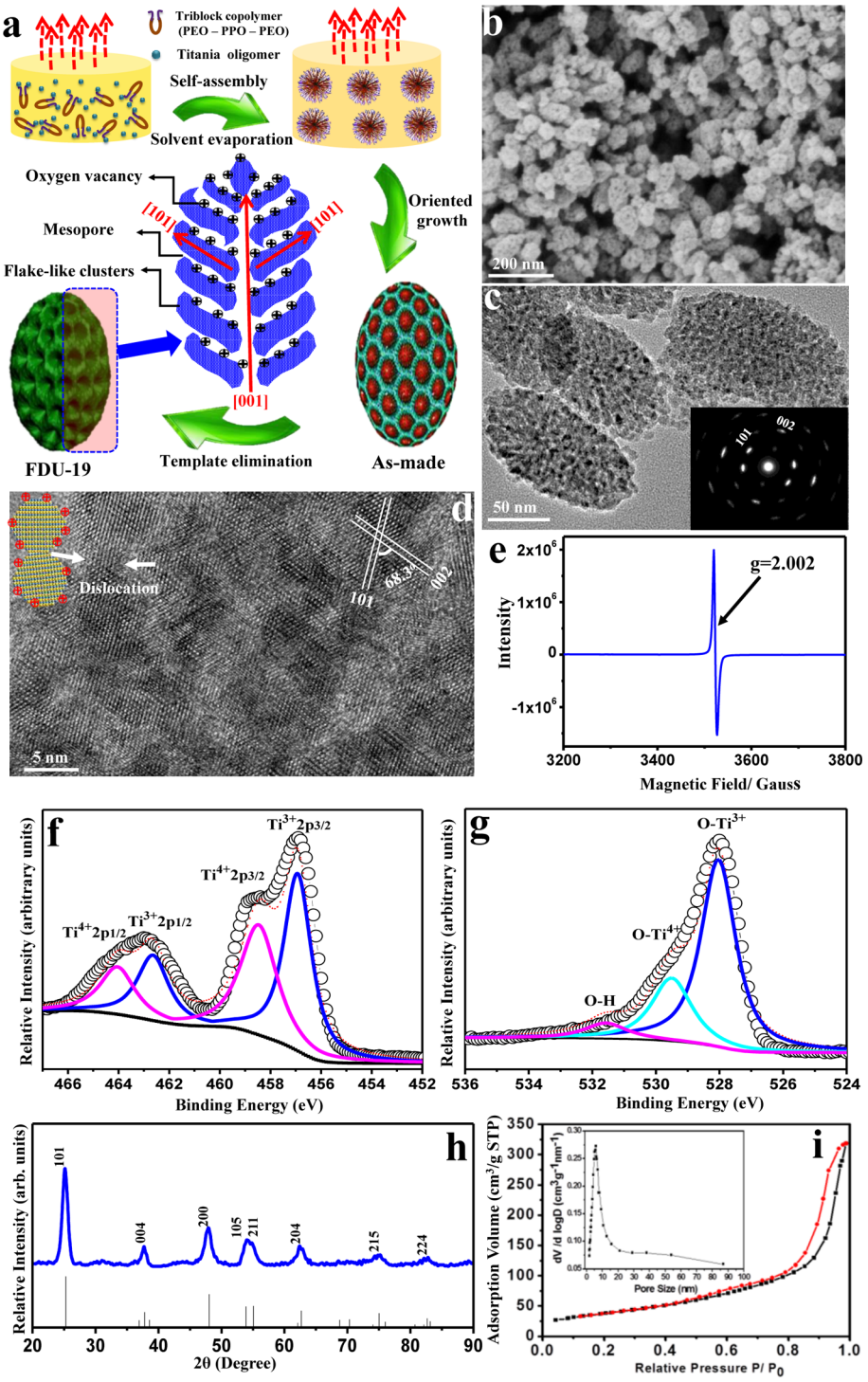

Figure 1. Formation and characterization of the mesoporous TiO_2 mesocrystals (FDU-19). (a) Schematic representation of the formation process of the olive-like mesoporous TiO_2 mesocrystals through the evaporation-driven oriented assembly process. (b) SEM image of the mesoporous TiO_2 mesocrystals FDU-19. (c) TEM images of the FDU-19 mesocrystals, recorded along the [010] axis. Inset (c) is the SAED pattern of an individual mesocrystal. (d) HRTEM image of an individual FDU-19 mesocrystal recorded along the [010] axis. Inset (d) is the structural model of the dislocation within mesocrystals FDU-19. (e) The electron paramagnetic resonance (EPR) spectra of the mesoporous mesocrystals FDU-19, recorded at room temperature (25 °C). (f) Ti_{2p} XPS core-level spectra for FDU-19. (g) O_{1s} XPS core-level spectra for FDU-19. (h) WXRD pattern of the mesoporous mesocrystals, compared to the standard anatase (space group $I4_1/amd$, JCPDS card No. 21-1272). (i) Nitrogen adsorption−desorption isotherms and pore size distributions (inset) of the olive-shaped mesoporous mesocrystals FDU-19. The pore size distributions are determined by the Barrett−Joyner−Halenda (BJH) model based on the respective absorption branches.

size of the mesocrystals FDU-19 can be well tuned from 80 to 200 nm by simply varying the concentration of the precursor solution.

After the annealing of the mesocrystals FDU-19 in air at 400 °C for 3 h again, SEM and TEM images reveal that the flake-like anatase building blocks can completely be fused into

DOI: 10.1021/acscentsci.5b00256
ACS Cent. Sci. 2015, 1, 400−408

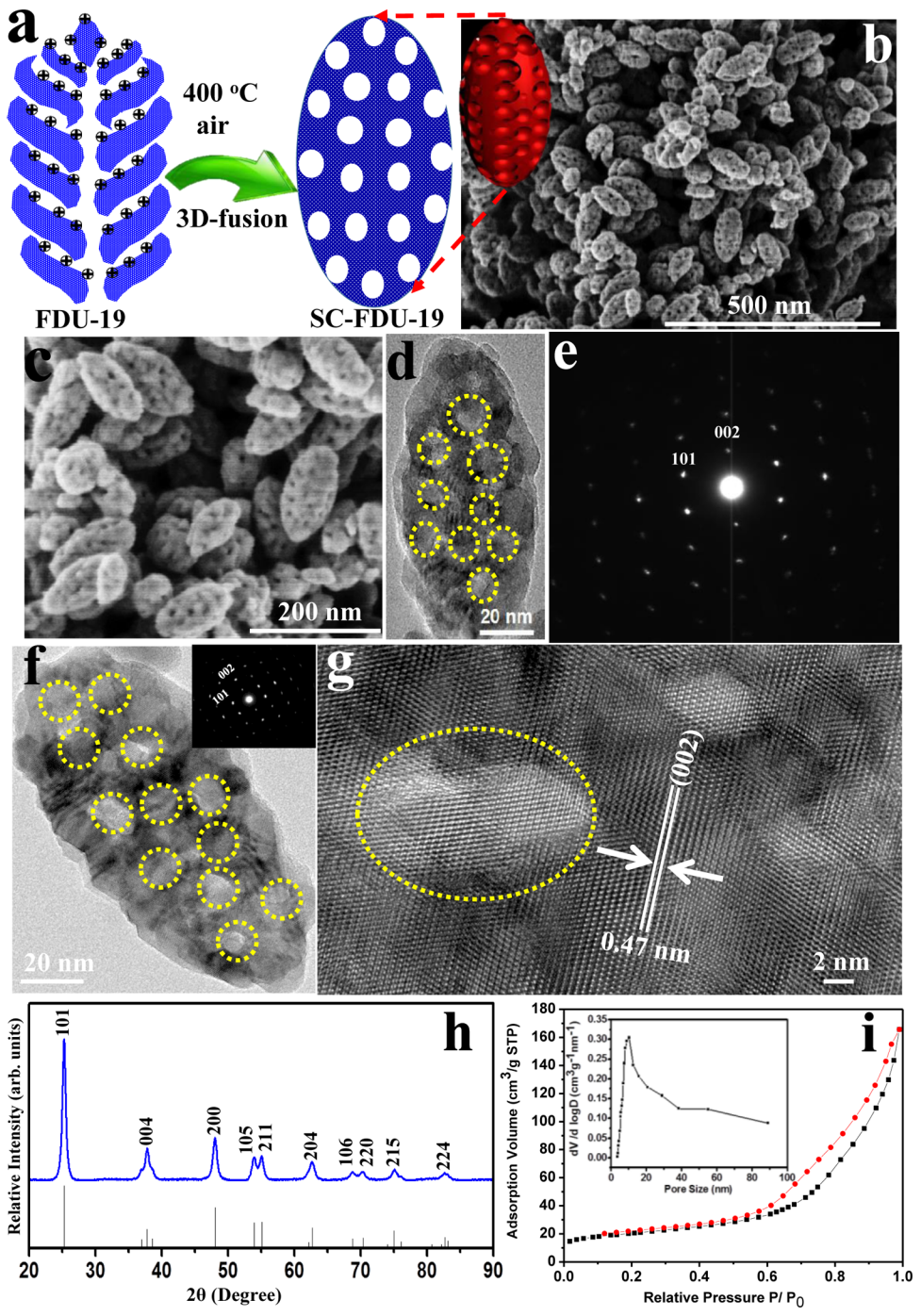

Figure 2. Formation and characterization of 3D-open mesoporous TiO_2 single crystals (SC-FDU-19). (a) Schematic representation of the formation process of the olive-shaped mesoporous TiO_2 single-crystals SC-FDU-19 after heat treating in air at 400 °C. (b, c) SEM images of the mesoporous single-crystals SC-FDU-19. (d) TEM images of a perpendicular mesoporous single-crystals SC-FDU-19 recorded along the [010] axis; (e) SAED patterns of an individual single-crystal SC-FDU-19 shown in (d); (f) TEM images of a slant mesoporous single crystals SC-FDU-19 recorded along the [010] axis; inset (f) is the corresponding SAED patterns of SC-FDU-19 shown in (f); (g) HRTEM image of an individual mesoporous TiO_2 single-crystal SC-FDU-19 recorded along the [010] axis; (h) WXRD pattern of the olive-like TiO_2 single-crystals SC-FDU-19, compared to the standard anatase (space group $I4_1/amd$, JCPDS card No. 21-1272). (i) Nitrogen adsorption−desorption isotherms and pore size distributions (inset) of the mesoporous TiO_2 single crystals.

structural-defect-free mesoporous anatase single-crystals (SC-FDU-19) along the [001] crystallographic axes (Figure 2 and Figure S7). Meanwhile, the olive-like morphology is retained, and the mesopore channels of the mesocrystals FUD-19 are changed to 3D open spherical mesopores throughout the whole particles (Figure 2a−c and Figure S8). The pore size is roughly estimated to be ∼14 nm, about two times larger than that of FDU-19 mesocrystals, implying a 3D merging of the neighbor mesochannels. TEM images and SAED patterns recorded along the [010] zone (Figure 2d−g and Figure S9) confirm the single-crystalline characteristics of SC-FDU-19 nanoparticles. HRTEM images recorded on a single particle (Figure 2g and Figure S9e) clearly show the perfect continuous 2D atomic lattices with spacings of 0.35 and 0.47 nm, corresponding to the (101) and (002) planes of anatase, respectively.

DOI: 10.1021/acscentsci.5b00256
ACS Cent. Sci. 2015, 1, 400−408

The XRD pattern (Figure 2h) shows that SC-FDU-19 nanoparticles retain a single-crystal anatase phase (space group $I4_1/amd$). Compared to that for the mesocrystals FDU-19, the BET surface area and pore volume of SC-FDU-19 decrease to 132 m^2/g and 0.278 cm^3/g (Figure 2i), respectively, but are still very high for the single-crystalline TiO_2. The pore size is measured to be about 14 nm (inset of Figure 2i), consistent with that from TEM results. XPS spectra of the mesoporous TiO_2 single-crystals SC-FDU-19 only show the lattice oxygen O−Ti^{4+} (Figure S10), and no lattice oxygen O−Ti^{3+} is found. The EPR data also show no oxygen vacancies or Ti^{3+} species (Figure S11). The results confirm that the unsaturated Ti^{3+} are completely oxidized to Ti^{4+} during the annealing process in air at 400 °C. The zeta potential is measured to be a pure positive value (+ 35 mV) (Figure S12). The average size of SC-FDU-19 mesoporous TiO_2 single-crystal nanoparticles can be well tuned from 80 to 140 nm by simply varying the original size of the as-made sample FDU-19 (Figures S13 and S14).

More significantly, after the mesocrystals FDU-19 were annealed in a vacuum (~4.0×10^{-5} Pa) at 400 °C for 2 h, the in situ TEM characterization reveals that the TiO_2 mesocrystals FDU-19 experience an abrupt 3D to 2D structural transformation to form free-standing ultrathin anatase single-crystal nanosheets (NS-FDU-19) (Figure 3a). The TEM image (Figure 3b) shows that the resultant NS-FDU-19 consists of well-faceted sheet-shaped nanostructures with an average size of about 80 nm. On the basis of the analysis of more than 50 nanosheets, the lateral thickness was measured to be ~8.3 nm, similar to that for the original flake-like nanocrystal building blocks of FDU-19. HRTEM images taken from a single sheet (Figure 3c−f) show a typical single-crystalline structure with two perpendicular sets of lattice facets corresponding to anatase (020) and (200) planes, suggesting that the top and bottom facets of NS-FDU-19 nanosheets are (001) planes. The lattice spacing parallel to the top and bottom facets is directly measured by TEM images to be 0.47 nm (Figure 3f), corresponding to the (002) plane of anatase. Assuming that each nanosheet is tetragonal in shape, one single sheet with ~8 nm in thickness and ~80 nm in size has ~90% of the exposed surfaces from the (001) facets.[31] The in situ Ti 2p XPS results of the NS-FDU-19 TiO_2 nanosheets show that the ratio of Ti^{3+}/ Ti^{4+} dramatically increases to 2.4:1 (Figure 3g,h). Correspondingly, O 1s spectra show mainly the lattice oxygen O−Ti^{3+} peak, and no trace of hydroxyl oxygen (O−H) is found (Figure 3h and Figure S15). Compared to mesoporous mesocrystals FDU-19, a much stronger EPR signal at g = 2.002 from oxygen vacancies on the surface of SC-FDU-19 is observed (Figure S16). The above XPS and EPR results clearly indicate that more oxygen vacancies are generated after removing the chemisorbed O_2, −OH, and H_2O from the surface of FDU-19 mesocrystals during the annealing process in a vacuum.

To further investigate the formation of NS-FDU-19, we followed up the growth trajectory of the TiO_2 nanosheets. In situ TEM characterization (Figure S17 and S18) reveals that the thermal activation under a high vacuum can first drive the flake-like nanocrystal building blocks to move freely, leading to their gradually detaching from FDU-19 mesocrystal particles. Instead of conventional 3D oriented attachment, these detached flake-like anatase nanocrystals undergo a continuous rotation and a 2D side-to-side oriented attachment. The continuous side-to-side attachment generates a free-standing ultrathin anatase single-crystal nanosheet (Figure S18c−f). It is also found that the lattice rotation and mass redistribution accompanied by structure relaxation proceed in such abrupt structural transformation. The real-time HRTEM image (Figure S19) clearly reveals an atom-to-atom reorientation via grain-boundary migration. It is remarkable that all TiO_2 nanosheets are grown by 2D side-to-side monolayer attachment, leaving (001) facets as the dominant exposed facets. In addition, in situ TEM images (Figure S20) also reveal that the freshly formed nanosheets are free-standing in a spherical symmetry, rather than conventional 3D aggregation, implying a strong anisotropic electrostatic repulsion between the NS-FDU-19 nanosheets.

The oriented growth of the olive-shaped FDU-19 mesocrystals is related to the solvent evaporation driven-oriented assembly process from two solvents with different boiling-point (THF and water). At the first stage, the spherical PEO−PPO−PEO/titania composite micelles are formed at the interface between the THF- and water-rich phases, minimizing the surface tension. With a continuous solvent evaporation at 60 °C, these small spherical composite micelles begin to an anisotropic aggregation in three dimensions (along the a- and c-axis) because of the different boiling points for the two solvents THF and water. The high-boiling-point water is preferentially evaporated up out, which makes a slow driving force along the c-axis (Figure S21), resulting in olive-shaped micelle aggregates. Finally, a center to outside evaporation of residual THF and water can cause fusing PEO−PPO-PEO/titania spherical micelles into curving cylindrical channel-like micelles along the free radial and restricted tangential direction, which is confirmed by the degraded broad small-angle X-ray scattering (SAXS) peaks (Figure S22). Correspondingly, such a center to outside evaporation force also drives TiO_2 oligomers cross-linked into flake-like nanocrstalline building blocks around F127 cylindrical micelles at a low temperature.

After the removal of the template by calcination under N_2 at 350 °C for 2 h, the flake-like crystals of the mesoporous mesocrystals FDU-19 are dominated by abundant oxygen vacancies on surface, inducing remarkable crystallite-interface reactivity. By capping defected crystal surfaces with chemisorbed oxygen species (e.g., O_2, −OH, and H_2O) in ambient environment, the mesoporous mesocrystals FDU-19 are stable with a large porosity.[43,44] During annealing in air, the adjacent nanocrystal building blocks can be further cross-linked by removing surface −OH groups, and the increasing oriented attractive forces can further lead to the 3D crystallographic fusion along the [001] direction, yielding the mesoporous single-crystals SC-FDU-19. It is reasonable to believe that such a 3D in situ fusion process is driven by the decrease in total system energy by reducing surface energy and eliminating the crystal defects. The thermal stability of TiO_2 mesocrystals is low due to pore walls consisting of ultrathin active flake-like building blocks. Upon calcination in air, the neighboring mesopores are interconnected and merged into condensed cage-type pores.

However, an abrupt 3D to 2D structural transformation from mesoporous mesocrystals to ultrathin anatase single-crystal nanosheets here is attributed to the enhanced anisotropic electrostatic interactions and dipole moments of the flake-like building blocks in a high vacuum. All flake-like nanocrystals within TiO_2 mesocrystals are mainly positive charged from the abundant surface oxygen vacancy defects. By annealing in a high vacuum environment, it can drive the surface-capping oxygen species completely desorbed from the defected surface, and more vacancies are therefore generated, further enhancing the anisotropic electrostatic repulsion and dipole moments between the adjacent flake-like nanocrystal building blocks within mesocrystals. Assuming that each building block is a distinct point

DOI: 10.1021/acscentsci.5b00256
ACS Cent. Sci. 2015, 1, 400−408

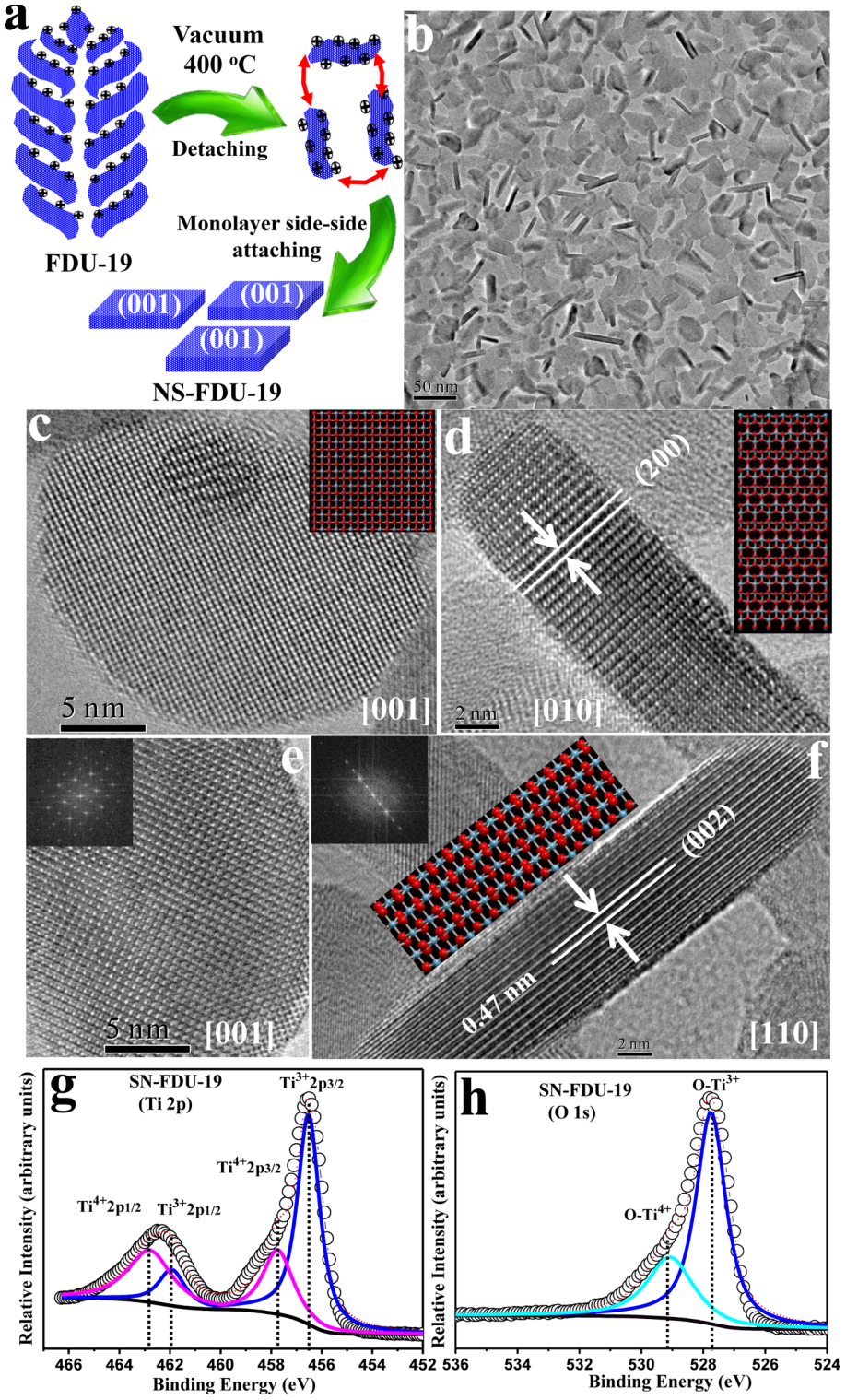

Figure 3. TEM characterization and XPS spectra of the ultrathin single-crystal TiO_2 nanosheets (NS-FDU-19). (a) Schematic representation of a monolayer attachment formation process for SN-FDU-19 nanosheets by heating in a vacuum (~4.0×10^{-5} Pa) at 400 °C. (b) TEM image of the obtained ultrathin SN-FDU-19 nanosheets. (c) HRTEM images of an individual TiO_2 nanosheet recorded along the [001] axis. Inset (c) is the corresponding crystallographic structure of the (001) surface. Ti and O atoms are represented by blue and red spheres, respectively; (d), HRTEM image of an individual nanosheet SC-FDU-19 recorded along the [010] axis. Inset (d) is the corresponding crystallographic structure of the (010) surface; (f) HRTEM image of an individual nanosheet SC-FDU-19 recorded along the [110] axis. Inset (f) is the corresponding crystallographic structure of (110) surface; the top left insets of (e, f) are the corresponding FFT patterns recorded on the (001) and (110) surface, respectively. (g) Ti 2p XPS core-level spectra for SN-FDU-19. (h) O 1s XPS core-level spectra for SN-FDU-19.

electric dipole, our computer electrostatic interactions simulation shows that the lowest interaction energy state between these flake-like nanocrystalks is the 2D side−side monolayer alignments, rather than 3D bottom−bottom or bottom-side

DOI: 10.1021/acscentsci.5b00256
ACS Cent. Sci. 2015, 1, 400−408

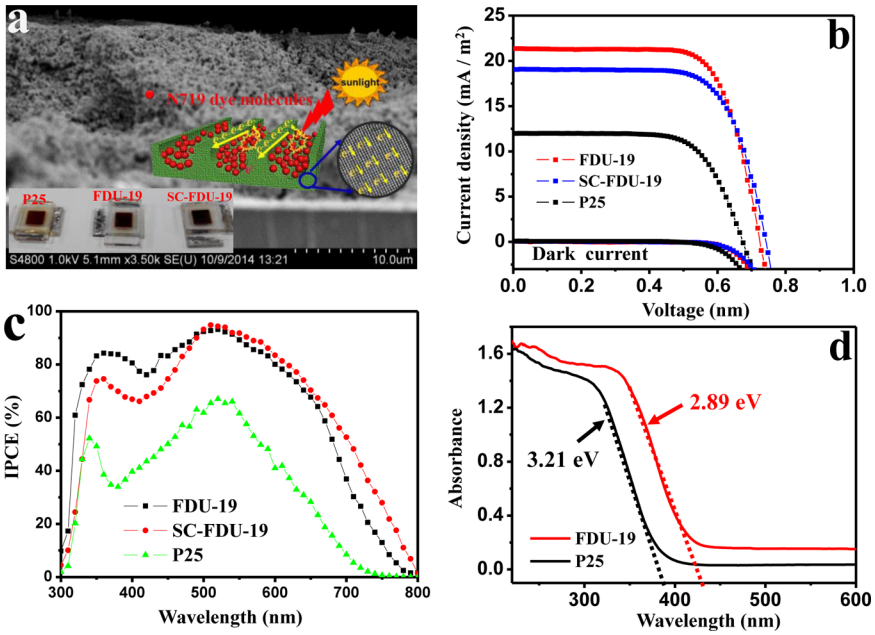

Figure 4. Photovoltaic device characterization. (a) The cross-section SEM image of a dye-sensitized solar cell (DSSC) comprised of the mesoporous mesocrystals FDU-19 with the film thickness of about 13.1 μm. Insets are the photographs of the three photovoltaic devices and schematic illustration of photogenerated electrons transmission within a mesoporous single-crystal TiO_2 wall. (b) $J-V$ curves of DSSCs fabricated from the three TiO_2 samples with dye N719 under AM 1.5 G simulated sunlight with a power density of 100 mW cm^{-2} and in the dark condition. The mesocrystals FUD-19 based photovoiltaic device shows the highest short-circuit photocurrent density (J_{sc}) of ~21.8 mA cm^{-2}, an open-circuit voltage (V_{oc}) of ~0.713 V, and a fill factor (FF) of ~0.748, yielding the highest η of 11.6%. (c) IPCE as a function of incident wavelength for the three TiO_2 samples: FDU-19, SC-FDU-19, P25. (d) Diffusive reflectance UV−vis spectrum of FDU-19 and P25.

aggregations (Figure S23). Thus, the flake-like nanocrystals can be gradually detached from the mother FDU-19 mesocrystals and further side−side self-reconstructed to ultrathin anatase single-crystal nanosheets.

The mesoporous TiO_2 materials were tested for the dye-sensitized solar cells (DSSCs) application. The cross-section SEM image of a typical mesoporous mesocrystal FDU-19 based-film device prepared by screen printing technology (Figure 4a) shows that the film thickness is about 13 μm. The photocurrent density (J)−voltage (V) curve (Figure 4b) for the DSSCs fabricated from the mesoporous TiO_2 mesocrystals exhibits an ultrahigh short-circuit photocurrent density (J_{sc}) of ~21.8 mA cm^{-2}, an open-circuit voltage (V_{oc}) of ~0.713 V, and a fill factor (FF) of ~0.748, yielding a very high power conversion efficiency (PCE) of 11.6%. Meanwhile, the DSSC device based on the mesoporous TiO_2 single-crystal nanoparticles SC-FDU-19 shows J_{sc} = 21.4 mA cm^{-2}, V_{oc} = 0.727 V, and FF = 0.731, resulting that PCE is as high as 11.3%. In contrast, the best PCE is measured to be only ~6.3% for commercial Degussa TiO_2 P25 under the same standard AM 1.5 sunlight illumination. The FDU-19 and SC-FDU-19 based photovoltaic cells show unprecedented power conversion efficiencies over 11%, which is comparable to those of todaýs best TiO_2-based thin film photovoltaic devices (Table S1). Moreover, the unwanted dark current density of P25-based DSSC is higher than that of the mesoporous FDU-19 mesocrystals and mesoporous SC-FDU-19 single-crystals-based DSSC at the same potential above 0.6 V (Figure 4b), suggesting that the latters have lower charge recombination rate than the former. The incident photo-to-current conversion efficiencies (IPCE) of the mesoporous mesocrystals exceed 60% in a broad spectral range from 450 to 650 nm, reaching its maximum of about 92% at 525 nm (Figure 4c). The photoresponse region was remarkably extended over 800 nm for the DSSC based on the mesocrystals FDU-19. Such an expanded photoresponsive behavior is attributed to the large amount of unsaturated Ti^{3+} sites within the mesoporous mesocrystals FDU-19. From the overlap integral with the standard global AM 1.5 solar emission spectra, the integrated photocurrent density from the IPCE spectrum for the mesocrystals FDU-19 was calculated to be 19.34 mA/cm^2, which is 88.5% of the measured J_{sc} value (21.8 mA/cm^2). The experimental J_{sc} error between the $J-V$ curve and IPCE was ~11.5%. This is probably due to the spectral mismatch between the two simulated solar lights in the two separated instruments. Diffusive reflectance UV−vis spectroscopy (Figure 4d) revealed that the optical bandgap of FDU-19 was 2.89 eV, which is about 0.3 eV lower than that of Degussa P25, which is substantially narrowed by abundant Ti^{3+} sites. The low bandgap of FDU-19 can enhance the visible- and infrared-light absorption, which is an important factor for the high photoconversion efficiency of FDU-19.[45−47]

The loading capacity of commercial dye N719 for FDU-19 mesocrystals is about 5.7×10^{-7} mol cm^{-2} (5.4×10^{-7} mol cm^{-2} for mesoporous TiO_2 single-crystals SC-FDU-19), about five times higher than that of P25 (1.12×10^{-7} mol cm^{-2}). The Nyquist plots of EIS for the three DSSCs show two well-defined semicircles in the high (>1 kHz) and medium frequency regions (1−100 Hz), respectively. The recombination resistance (Rct) of FDU-19 mesocrystals, SC-FDU-19 single-crystals and P25 is 85.9, 87.1, and 26.4 Ω, and the corresponding electron lifetime (τ_r) is calculated to be about 128, 134, and 53 ms, respectively. The above EIS results well confirm that the FDU-19 meso-crystals and SC-FDU-19 single crystals-based DSSCs have lower charge recombination rate than that of P25. On the basis of the above DSSCs characterization, the high efficiencies of FDU-19 and SC-FDU-19 based-cells can be well understood as the results of the large amount of oxygen vacancies, high surface area and

DOI: 10.1021/acscentsci.5b00256
ACS Cent. Sci. 2015, 1, 400−408

Table 1. Photovoltaic Parameters of DSSCs Based on the Photoanodes of the Mesoporous TiO_2 Mesocrystals (FDU-19), Olive-Shaped Mesoporous TiO_2 Single Crystals (SC-FDU-19) and Commercial P25[a]

samples	Voc [mV]	Jsc [mA cm^2]	FF[%]	η [%]	adsorbed dye [$\times 10^{-7}$ mol cm^{-2}][b]
FDU-19	713	21.8	74.8	11.6	5.7
SC-FDU-19	727	21.4	73.1	11.3	5.4
P25	710	11.9	74.5	6.3	1.1

[a]After $TiCl_4$ post-treatments, which were measured under AM 1.5 sunlight illumination (100 mW cm^{-2}). The active area of the device with a metal mask was about 0.16 cm^2. [b]The dye-adsorbed films with an area of ~10 cm^2 were used for estimating the adsorbed dye concentration. The commercial N719 dye was first desorbed into a 0.1 M NaOH solution in water and ethanol (1:1, *V/V*), and then the desorbed-N719 dye concentration was measured by using UV−vis spectrophotometer.

porosity, low band gap, and fast electron transfer through the single-crystalline anatase walls with large mesopores.

It is noted here that the single-crystal nanosheets NS-FDU-19 with a high percentage of reactive (001) facets shows ultrahigh performance in photocatalytic reactions (Figure S23). The photocatalytic decomposition of methylene blue dye ($1\ 0 \times 10^{-4}$ mol L^{-1}, 50 mL) over NS-FDU-19 nanosheets could be completed in 8 min under a simulated sunlight irradiation ($200 < \lambda < 800$ nm), which was five times faster than that over P25. The excellent photocatalytic performance of the NS-FDU-19 nanosheets can be attributed to the large number of the oxygen vacancies located on the surface and high percentage of reactive (001) facets. The well-defined single-crystal nanosheets NS-FDU-19 synthesized in this work are also expected as a model single-crystal for fundamental studies in surface science.

■ ASSOCIATED CONTENT

Supporting Information

The Supporting Information is available free of charge on the ACS Publications website at DOI: 10.1021/acscentsci.5b00256.

Experimental materials and methods, more detailed characterizations and discussions (PDF)

■ AUTHOR INFORMATION

Corresponding Author

*E-mail: dyzhao@fudan.edu.cn. Web: http://www.mesogroup.fudan.edu.cn/.

Notes

The authors declare no competing financial interest.

■ ACKNOWLEDGMENTS

This work is supported by the State Key Basic Research Program of China (2013CB934104 and 2012CB224805), the National Science Foundation (21210004) and Science & Technology Commission of Shanghai Municipality (14JC1400700), Shanghai Leading Academic Discipline Project (B108), and Deanship of Scientific Research, KSU-The International Highly Cited Research Group program (IHCRG#14-102). Y.L. also acknowledges the Interdisciplinary Outstanding Doctoral Research Funding of Fudan University (EZH2203302/001).

■ REFERENCES

(1) Suteewong, T.; Sai, H.; Hovden, R.; Muller, D.; Bradbury, M. S.; Gruner, S. M.; Wiesner, U. Multicompartment mesoporous silica nanoparticles with branched shapes: An epitaxial growth mechanism. *Science* **2013**, *340*, 337−341.

(2) Djojoputro, H.; Zhou, X.; Qiao, S.; Wang, L.; Yu, C.; Lu, G. Periodic mesoporous organosilica hollow spheres with tunable wall thickness. *J. Am. Chem. Soc.* **2006**, *128*, 6320−6321.

(3) Qiao, S.; Yu, C.; Xing, W.; Hu, Q.; Djojoputro, H.; Lu, G. Synthesis and bio-adsorptive properties of large-pore periodic mesoporous organosilica rods. *Chem. Mater.* **2005**, *17*, 6172−6176.

(4) Lou, X. W. D.; Archer, L. A.; Yang, Z. Hollow micro/nanostructures: synthesis and applications. *Adv. Mater.* **2008**, *20*, 3987−4019.

(5) Liu, B.; Liu, L.-M.; Lang, X.-F.; Wang, H.-Y.; Lou, X. W.; Aydil, E. S. Doping high-surface-area mesoporous TiO_2 microspheres with carbonate for visible light hydrogen production. *Energy Environ. Sci.* **2014**, *7*, 2592−2597.

(6) Chen, J. S.; Liu, J.; Qiao, S. Z.; Xu, R.; Lou, X. W. Formation of large 2D nanosheets via PVP-assisted assembly of anatase TiO2 nanomosaics. *Chem. Commun.* **2011**, *47*, 10443−10445.

(7) Kuang, Q.; Yang, S. Template Synthesis of Single-Crystal-Like Porous $SrTiO_3$ Nanocube Assemblies and Their Enhanced Photocatalytic Hydrogen Evolution. *ACS Appl. Mater. Interfaces* **2013**, *5*, 3683−3690.

(8) Liu, H.; Su, D.; Zhou, R.; Sun, B.; Wang, G.; Qiao, S. Z. Highly Ordered Mesoporous MoS_2 with Expanded Spacing of the (002) Crystal Plane for Ultrafast Lithium Ion Storage. *Adv. Energy Mater.* **2012**, *2*, 970−975.

(9) Liu, H.; Wang, G.; Liu, J.; Qiao, S.; Ahn, H. Highly ordered mesoporous NiO anode material for lithium ion batteries with an excellent electrochemical performance. *J. Mater. Chem.* **2011**, *21*, 3046−3052.

(10) Yang, H.; Coombs, N.; Sokolov, I.; Ozin, G. A. Free-standing and oriented mesoporous silica films grown at the air-water interface. *Nature* **1996**, *381*, 589−592.

(11) Cölfen, H.; Antonietti, M. Mesocrystals: inorganic superstructures made by highly parallel crystallization and controlled alignment. *Angew. Chem., Int. Ed.* **2005**, *44*, 5576−5591.

(12) De Yoreo, J. J.; Gilbert, P. U. P. A.; Sommerdijk, N. A. J. M.; Penn, R. L.; Whitelam, S.; Joester, D.; Zhang, H.; Rimer, J. D.; Navrotsky, A.; Banfield, J. F.; Wallace, A. F.; Michel, F. M.; Meldrum, F. C.; Cölfen, H.; Dove, P. M. Crystallization by particle attachment in synthetic, biogenic, and geologic environments. *Science* **2015**, *349*, 498.

(13) Fang, J.; Ding, B.; Gleiter, H. Mesocrystals: Syntheses in metals and applications. *Chem. Soc. Rev.* **2011**, *40*, 5347−5360.

(14) Niederberger, M.; Cölfen, H. Oriented attachment and mesocrystals: Non-classical crystallization mechanisms based on nanoparticle assembly. *Phys. Chem. Chem. Phys.* **2006**, *8*, 3271−3287.

(15) Li, M.; Schnablegger, H.; Mann, S. Coupled synthesis and self-assembly of nanoparticles to give structures with controlled organization. *Nature* **1999**, *402*, 393−395.

(16) Davis, M. E. Ordered porous materials for emerging applications. *Nature* **2002**, *417*, 813−821.

(17) Tian, B.; Liu, X.; Tu, B.; Yu, C.; Fan, J.; Wang, L.; Xie, S.; Stucky, G. D.; Zhao, D. Self-adjusted synthesis of ordered stable mesoporous minerals by acid−base pairs. *Nat. Mater.* **2003**, *2*, 159−163.

(18) Lu, Y.; Fan, H.; Stump, A.; Ward, T. L.; Rieker, T.; Brinker, C. J. Aerosol-assisted self-assembly of mesostructured spherical nanoparticles. *Nature* **1999**, *398*, 223−226.

(19) Inagaki, S.; Guan, S.; Ohsuna, T.; Terasaki, O. An ordered mesoporous organosilica hybrid material with a crystal-like wall structure. *Nature* **2002**, *416*, 304−307.

(20) Fang, J.; Ding, B.; Gleiter, H. Mesocrystals: Syntheses in metals and applications. *Chem. Soc. Rev.* **2011**, *40*, 5347−5360.

(21) Liu, Y.; Che, R.; Chen, G.; Fan, J.; Sun, Z.; Wu, Z.; Wang, M.; Li, B.; Wei, J.; Wei, Y.; et al. Radially oriented mesoporous TiO_2 microspheres with single-crystal−like anatase walls for high-efficiency optoelectronic devices. *Sci. Adv.* **2015**, *1*, e1500166.

(22) Ye, J.; Liu, W.; Cai, J.; Chen, S.; Zhao, X.; Zhou, H.; Qi, L. Nanoporous anatase TiO_2 mesocrystals: additive-free synthesis,

DOI: 10.1021/acscentsci.5b00256
ACS Cent. Sci. 2015, 1, 400−408

remarkable crystalline-phase stability, and improved lithium insertion behavior. *J. Am. Chem. Soc.* **2011**, *133*, 933−940.
(23) Hong, Z.; Wei, M.; Lan, T.; Jiang, L.; Cao, G. Additive-free synthesis of unique TiO_2 mesocrystals with enhanced lithium-ion intercalation properties. *Energy Environ. Sci.* **2012**, *5*, 5408−5413.
(24) Crossland, E. J.; Noel, N.; Sivaram, V.; Leijtens, T.; Alexander-Webber, J. A.; Snaith, H. J. Mesoporous TiO_2 single crystals delivering enhanced mobility and optoelectronic device performance. *Nature* **2013**, *495*, 215−219.
(25) Song, R. Q.; Cölfen, H. Mesocrystals—ordered nanoparticle superstructures. *Adv. Mater.* **2010**, *22*, 1301−1330.
(26) Yang, H. G.; Sun, C. H.; Qiao, S. Z.; Zou, J.; Liu, G.; Smith, S. C.; Cheng, H. M.; Lu, G. Q. Anatase TiO_2 single crystals with a large percentage of reactive facets. *Nature* **2008**, *453*, 638−641.
(27) Yang, H. G.; Liu, G.; Qiao, S. Z.; Sun, C. H.; Jin, Y. G.; Smith, S. C.; Zou, J.; Cheng, H. M.; Lu, G. Q. Solvothermal synthesis and photoreactivity of anatase TiO_2 nanosheets with dominant {001} facets. *J. Am. Chem. Soc.* **2009**, *131*, 4078−4083.
(28) Chen, J. S.; Archer, L. A.; Lou, X. W. SnO_2 hollow structures and TiO_2 nanosheets for lithium-ion batteries. *J. Mater. Chem.* **2011**, *21*, 9912−9924.
(29) Chen, J. S.; Tan, Y. L.; Li, C. M.; Cheah, Y. L.; Luan, D.; Madhavi, S.; Boey, F. Y. C.; Archer, L. A.; Lou, X. W. Constructing Hierarchical Spheres from Large Ultrathin Anatase TiO_2 Nanosheets with Nearly 100% Exposed (001) Facets for Fast Reversible Lithium Storage. *J. Am. Chem. Soc.* **2010**, *132*, 6124−6130.
(30) Chen, J. S.; Chen, C.; Liu, J.; Xu, R.; Qiao, S. Z.; Lou, X. W. Ellipsoidal hollow nanostructures assembled from anatase TiO_2 nanosheets as a magnetically separable photocatalyst. *Chem. Commun.* **2011**, *47*, 2631−2633.
(31) Chen, J. S.; Tan, Y. L.; Li, C. M.; Cheah, Y. L.; Luan, D.; Madhavi, S.; Boey, F. Y. C.; Archer, L. A.; Lou, X. W. Constructing hierarchical spheres from large ultrathin anatase TiO_2 nanosheets with nearly 100% exposed (001) facets for fast reversible lithium storage. *J. Am. Chem. Soc.* **2010**, *132*, 6124−6130.
(32) Song, R.-Q.; Cölfen, H. Mesocrystals-Ordered Nanoparticle Superstructures. *Adv. Mater.* **2010**, *22*, 1301−1330.
(33) Wang, T. X.; Cölfen, H.; Antonietti, M. Nonclassical crystallization: Mesocrystals and morphology change of $CaCO_3$ crystals in the presence of a polyelectrolyte additive. *J. Am. Chem. Soc.* **2005**, *127*, 3246−3247.
(34) Xu, A.-W.; Antonietti, M.; Cölfen, H.; Fang, Y.-P. Uniform hexagonal plates of vaterite $CaCO_3$ mesocrystals formed by biomimetic mineralization. *Adv. Funct. Mater.* **2006**, *16*, 903−908.
(35) Ye, J.; Liu, W.; Cai, J.; Chen, S.; Zhao, X.; Zhou, H.; Qi, L. Nanoporous Anatase TiO_2 Mesocrystals: Additive-Free Synthesis, Remarkable Crystalline-Phase Stability, and Improved Lithium Insertion Behavior. *J. Am. Chem. Soc.* **2011**, *133*, 933−940.
(36) Zhou, L.; O'Brien, P. Mesocrystals: A New Class of Solid Materials. *Small* **2008**, *4*, 1566−1574.
(37) Zuo, F.; Wang, L.; Wu, T.; Zhang, Z.; Borchardt, D.; Feng, P. Self-doped Ti^{3+} enhanced photocatalyst for hydrogen production under visible light. *J. Am. Chem. Soc.* **2010**, *132*, 11856−11857.
(38) Kumar, P. M.; Badrinarayanan, S.; Sastry, M. Nanocrystalline TiO_2 studied by optical, FTIR and X-ray photoelectron spectroscopy: correlation to presence of surface states. *Thin Solid Films* **2000**, *358*, 122−130.
(39) Lu, X. H.; Wang, G. M.; Zhai, T.; Yu, M. H.; Gan, J. Y.; Tong, Y. X.; Li, Y. Hydrogenated TiO_2 nanotube arrays for super capacitors. *Nano Lett.* **2012**, *12*, 1690−1696.
(40) Liu, Y.; Chen, L.; Hu, J.; Li, J.; Richards, R. TiO_2 Nanoflakes Modified with Gold Nanoparticles as Photocatalysts with High Activity and Durability under near UV Irradiation. *J. Phys. Chem. C* **2010**, *114*, 1641−1645.
(41) Liu, Y.; Deng, Y.; Sun, Z.; Wei, J.; Zheng, G.; Asiri, A. M.; Khan, S. B.; Rahman, M. M.; Zhao, D. Hierarchical Cu_2S Microsponges Constructed from Nanosheets for Efficient Photocatalysis. *Small* **2013**, *9*, 2702−2708.
(42) Evans, J.; Hayden, B.; Mosselmans, F.; Murray, A. The chemistry of rhodium on TiO_2 (110) deposited by MOCVD of $[Rh(CO)_2Cl]_2$ and MVD. *Surf. Sci.* **1994**, *301*, 61−82.
(43) Setvín, M.; Aschauer, U.; Scheiber, P.; Li, Y.-F.; Hou, W.; Schmid, M.; Selloni, A.; Diebold, U. Reaction of O_2 with subsurface oxygen vacancies on TiO_2 anatase (101). *Science* **2013**, *341*, 988−991.
(44) Tang, Z.; Zhang, Z.; Wang, Y.; Glotzer, S. C.; Kotov, N. A. Self-assembly of CdTe nanocrystals into free-floating sheets. *Science* **2006**, *314*, 274−278.
(45) Chen, X.; Liu, L.; Yu, P. Y.; Mao, S. S. Increasing Solar Absorption for Photocatalysis with Black Hydrogenated Titanium Dioxide Nanocrystals. *Science* **2011**, *331*, 746−750.
(46) Naldoni, A.; Allieta, M.; Santangelo, S.; Marelli, M.; Fabbri, F.; Cappelli, S.; Bianchi, C. L.; Psaro, R.; Dal Santo, V. Effect of Nature and Location of Defects on Bandgap Narrowing in Black TiO_2 Nanoparticles. *J. Am. Chem. Soc.* **2012**, *134*, 7600−7603.
(47) Hu, Y. H. A Highly Efficient Photocatalyst Hydrogenated Black TiO_2 for the Photocatalytic Splitting of Water. *Angew. Chem., Int. Ed.* **2012**, *51*, 12410−12412.

DOI: 10.1021/acscentsci.5b00256
ACS Cent. Sci. 2015, 1, 400−408